Acta Biomaterialia 51 (2017) 393–407

Contents lists available at ScienceDirect

Acta Biomaterialia

journal homepage: www.elsevier.com/locate/actabiomat

Full length article

Structure and mechanical implications of the pectoral fin skeleton in the Longnose Skate (Chondrichthyes, Batoidea)

Wei Huang [a,*], Watcharapong Hongjamrassilp [b], Jae-Young Jung [a], Philip A. Hastings [b], Vlado A. Lubarda [a,c], Joanna McKittrick [a,d]

[a] Materials Science and Engineering Program, University of California, San Diego, La Jolla, CA 92093, United States
[b] Scripps Institution of Oceanography, University of California, San Diego, La Jolla, CA 92093, United States
[c] Department of Nanoengineering, University of California, San Diego, La Jolla, CA 92093, United States
[d] Department of Mechanical and Aerospace Engineering, University of California, San Diego, La Jolla, CA 92093, United States

ARTICLE INFO

Article history:
Received 29 July 2016
Received in revised form 16 December 2016
Accepted 5 January 2017
Available online 6 January 2017

Keywords:
Batoid fins
Undulation swimming
Hierarchical structure
Mineralized cartilage
Mechanical properties

ABSTRACT

Animal propulsion systems are believed to show high energy and mechanical efficiency in assisting movement compared to artificial designs. As an example, batoid fishes have very light cartilaginous skeletons that facilitate their elegant swimming via enlarged wing-like pectoral fins. The aim of this work is to illustrate the hierarchical structure of the pectoral fin of a representative batoid, the Longnose Skate (*Raja rhina*), and explain the mechanical implications of its structural design. At the macro level, the pectoral fins are comprised of radially oriented fin rays, formed by staggered mineralized skeletal elements stacked end-to-end. At the micro level, the midsection of each radial element is composed of three mineralized components, which consist of discrete segments (tesserae) that are mineralized cartilage and embedded in unmineralized cartilage. The radial elements are wrapped with aligned, unmineralized collagen fibers. This is the first report of the detailed structure of the ray elements, including the observation of a 3-chain mineralized tesserae. Structural analyses demonstrate that this configuration enhances stiffness in multiple directions. A two-dimensional numerical model based on the morphological analysis demonstrated that the tessera structure helps distributing shear, tensile and compressive stress more ideally, which can better support both lift and thrust forces when swimming without losing flexibility.

Statement of Significance

Batoid fishes have very light cartilaginous skeletons that facilitate their elegant swimming by applying their enlarged wing-like pectoral fins. Previous studies have shown structural features and mechanical properties of the mineralized cartilage skeleton in various batoid fishes. However, the details of the pectoral fin structure at different length scales, as well as the relationship between the mechanical properties and structural design remains unknown. The present work illustrates the hierarchical structure of the pectoral fin of the Longnose Skate (a representative batoid fish) and verifies the materials configuration and structural design increases the stiffness of fin skeleton without a loss in flexibility. These results have implications for the design of strong but flexible materials and bio-inspired autonomous underwater vehicles (AUVs).

1. Introduction

After ~530 million years of evolution, the propulsion systems in more than 30,000 extant fish species show remarkable variability and efficiency in swimming in aquatic environments [1–3]. Batoidea is a lineage of cartilaginous fishes, including rays, skates and their relatives, and are distinguished by dorsoventrally flattened bodies and enlarged pectoral fins that are contiguous with the head. These wing-like fins are the main apparatus for batoid (ray) propulsion, termed rajiform swimming [4,5]. The movement trajectories of their pectoral fins during swimming vary in the number and frequency of undulatory waves that pass along the margin of the pectoral fins [6]. Among fish propulsion systems, swimming mechanisms with pectoral fins in batoid fish species have motivated research interests in developing promising

* Corresponding author.
E-mail address: w7huang@eng.ucsd.edu (W. Huang).

http://dx.doi.org/10.1016/j.actbio.2017.01.026
1742-7061/

bio-inspired autonomous underwater vehicles (AUVs) [7,8]. Moreover, by combining rat cardiomyocytes with artificial batoid skeleton, Park *et al.* [9] realized the efficient undulatory swimming on a tissue-engineered biohybrid robotic ray using optical stimulation.

Specific mechanical requirements are needed to meet the demands of propulsion. Since batoid fish swim primarily by undulating their pectoral fins, the fin should be not only flexible enough to form the undulatory waves along the distal margin of the fins, but also strong enough to resist the hydrodynamic propulsive force applied by the water environment [10]. The pectoral fins comprise radially oriented fin rays, which are composed of 10′s–100′s (depending on the fish size) of mineralized cartilage segments (radial elements), stacked end-to-end, connected by joints, similar to the phalangeal bones within the fingers of primates [11]. Fig. 1a shows schematic diagrams of a batoid fish with an expanded view of the fin ray elements and surrounding tissues. Calcified cartilage, identified in the skeletons of Chondrichthyes, is termed as endoskeletal tesserae, which are discrete blocks of calcified tissue that enhances the rigidity of the cartilaginous skeletons [11–20]. Schaefer and Summers [11] divided the tessera arrangements found in a variety of batoids into 'crustal,' indicating a complete tessellated layer, and 'catenated,' where tesserae instead form a chain-like pattern arranged in series along the length of the radial element. The catenated tesserae were further divided into 2-chain and 4-chain patterns. Two mineralized tessera chains located near dorsal and ventral surfaces of the radial element separately form the 2-chain pattern, while four chains distributed near all four surfaces (ventral, dorsal, medial, lateral) form the 4-chain pattern. A schematic illustration (Fig. 1b) shows the different patterns of tesserae (orange color) in longitudinal and cross-sectional in three representative species: crustal in the Thornback guitarfish (*Platyrhinoidis triseriata*), catenated 2-chain in the Thorny Skate (*Amblyraja radiata*) and catenated 4-chain in the Round Stingray (*Urobatis halleri*) [11]. In the crustal arrangement, the tesserae cover the entire outer surface, leaving the inner part with uncalcified cartilage (green color). While in the catenated patterns, the tesserae form 2 or 4 chains embedded in the uncalcified cartilage. It should be noted that in the catenated configurations, the chains finally form a palisaded tessellation pattern (numerous chains) at the ends of the radial element.

Sharks, as one representative member of Chondrichthyes, have a mineralized cartilage skeleton similar to the batoids [10,21,22]. Liu *et al.* [23] studied the mineralized cartilage structures in shark skeletons and found they consisted of a layer or layers of tesserae, sandwiched by a thin layer of unmineralized perichondrium with an unmineralized cartilage core. They proposed that there was a higher compressive than tensile stress distributed in the tesserae under excessive bending loads, which implied that the lower tensile stress protected the structure from tearing [23]. Tesserae morphology and anisotropic effects of blue shark jaw cartilage also have been analyzed [24]. The results show that the arrangement of tesserae relative to load has an effect on the mechanical behavior of the skeleton and therefore the arrangement of tesserae in the different radial morphologies may identify, for example, the loading conditions and kinematics. More importantly, the discrete calcified tiles can realize other specific functions such as protecting structure from bending loads and damping stress normal to the surface using this elastic anisotropy [23,25].

Although previous workers have studied details of the cartilage skeleton of the pectoral fins in various species of batoid fishes [11,26–28], the hierarchical structure of pectoral fin structure at different scale levels, as well as the relationship between the mechanical properties and structural design remains unknown. Although the wing-like structure of the pectoral fins of several species of batoid fishes has been studied, a more thorough understanding of the fin rays and radial anatomy, as well as their interactions with connective tissue and musculature can help to better understand this biocomposite propulsive system.

The present work examines the Longnose Skate, *Raja rhina*, as a research model, which is a representative species of the undulating swimming batoid fish found in the eastern Pacific from Alaska to Mexico. The study focuses on (1) characterizing of the hierarchical structure of pectoral fins, and (2) obtaining a better understanding of the relationships between the hierarchical structure and the mechanical behavior. We hypothesize that the structural designs can make the pectoral fin strong enough to withstand the propulsion forces without sacrificing flexibility. These hierarchical structures may give inspiration for the design of AUVs, and strong but flexible materials.

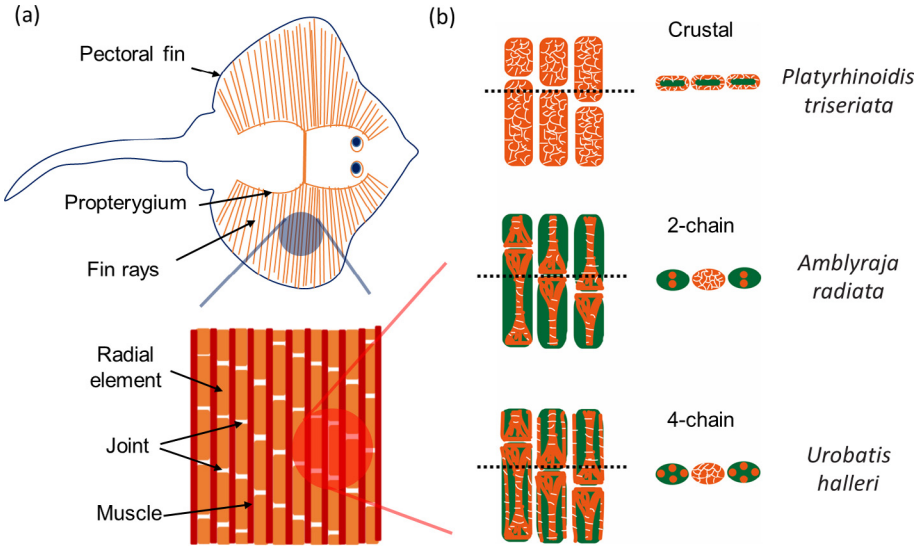

Fig. 1. Schematic of pectoral fin skeleton structure of batoid fish: (a) Pectoral fin skeleton structure. Fin rays and propterygium constitute pectoral fin skeleton. Discrete radial elements separated by joints in each fin ray. Muscle tissue connects adjacent fin rays; (b) Different tessera patterns in the radial element of three different batoid species. Schematics of longitudinal and cross sections of radial elements are shown correspondingly to different tessellation patterns. The orange color represents calcified materials, while green color represents unmineralized tissues. Crustal calcification exists in the Thornback guitarfish. Tesserae chains are shown in both the Round Stingray and Thorny Skate, indicating a catenated calcification pattern. Cross sections demonstrate 2-chains in the Thorny Skate and 4-chains in the Round Stingray. Adapted from [11].

2. Materials and methods

2.1. Sample collection

Three Longnose Skates were acquired from a ~340 m depth near the San Diego coastline during a Scripps Institution of Oceanography research cruise on April, 20, 2015. The specimens were collected under IACUC protocol S02118. The fish were immediately stored at −20 °C before further analysis.

2.2. X-ray images

Fresh specimens were radiographed using a Faxitron Model MX-20 cabinet radiography system (Tucson, AZ, USA) under 24 kV for 8 s with image plate. The image plate, which was exposed with X-ray radiation, was scanned in a ScanX-12 reader (Melville, NY, USA) to generate the X-ray image.

2.3. Micro-computed tomography (μ-CT)

Samples from the midsection of the pectoral fin were prepared by immersion in a saline solution to keep the whole structure hydrated. The pectoral fin skeleton was analyzed using a Skyscan 1076 μ-CT scanner (Bruker, Kontich, Belgium) with a 0.5 mm aluminum filter. The isotropic voxel size was 9 μm, the electric potential was 70 peak kV (kVp), and the current was 200 μA. After scanning, a post-scan beam hardening correction algorithm was applied during image reconstruction. Skyscan's Dataviewer and CTVox software (Bruker, Kontich, Belgium) was used to acquire images and Amira software (FEI Visualization Sciences Group, Burlington, MA) was used for 3D rendered models.

2.4. Histology

Radial elements were cut from pectoral fin samples of the Longnose Skate, and were fixed overnight in 4% formaldehyde solution. The samples then were decalcified in RDO rapid decalcifier (Apex Engineering Products Corporation, Aurora, IL) for 2 h. Once decalcified, the samples were transferred into a graded series of ethanol from 50%, 70%, 95%, to absolute ethanol for dehydration. The samples then were placed in xylene, which was changed every 20 min for three times before embedding in Paraplast (McCormick Scientific, St. Louis, MO). Finally, the samples were cut by a microtome into 5–7 μm sections and mounted on glass slide. Hematoxylin & Eosin (H&E) was used for staining. Optical microscopy images of stained slides were taken using Zeiss Axio imager equipped with CCD camera (Zeiss MicroImaging Inc., Thornwood, NY, USA) under transmitted light.

2.5. Scanning electron microscopy (SEM)

The fins were sectioned to extract several fin ray radial elements from the midsection of the fin. The radial elements were immersed in a 2.5 vol% glutaraldehyde solution for two hours to fix the structure. A graded series of ethanol solutions (20%, 40%, 60%, 80%, 95%, and 100% vol% ethanol) were applied to further dehydrate the samples. Some of the samples were then freeze-fractured after immersion in liquid nitrogen in both cross and longitudinal directions. Finally, a critical point dryer (Autosamdri-851, Tousimis, Rockville, MD, USA) was used to further remove the excess ethanol. The other samples were embedded in LR white resin (Electron Microscopy Sciences, PA, USA) and then polished to a flat surface. All the samples were sputter coated with iridium (Quorum Technologies Ltd., West Sussex, UK) before carrying out SEM imaging. Imaging was carried out with an ultra-high resolution microscope (FEI XL30, Hillsboro, OR, USA). During imaging, energy dispersive X-ray spectroscopy (EDS) and backscattering scanning electron microscopy (BSEM) were performed to acquire elemental compositions and mineral density.

2.6. Tensile tests

Tension testing was performed on nine fresh fin radial elements. Both skin and flesh surrounding the radial element was removed carefully by surgical knife. The fresh samples were stored in the refrigerator and kept in DI water ~2 h before testing. An instrumented load frame (Instron 3367, Instron Corporation, Norwood, MA, USA) with a load cell of 500 N was used to perform the tensile tests at a strain rate of 10^{-3} s^{-1}. Small pieces of sand paper were applied to glue the non-active areas of the samples to prevent sample sliding during tension and diminish local stress concentration. The gauge lengths of the samples were ~5 mm, which was the length of a single radial element. The cross section of the samples was assumed circular shape with diameters ~0.5 mm. The fractured surfaces of all the samples were imaged under SEM using the above procedure.

3. Results and discussion

3.1. Macrostructural characterization

Fig. 2a shows a photograph of a Longnose Skate, having a total length of ~25 cm and disc width of ~15 cm. The whole skeletal structure is shown in the X-ray image in Fig. 2b showing the connection of the pectoral fins to the propterygium support elements. As shown in a higher magnification X-ray image (Fig. 2c), the pectoral fin is composed of ~70 mineralized fin rays, which consist of series of radial elements connected end-to-end separated by a larger diameter joint. A staggered periodic pattern of the joints is observed, analogous to those reported for other rays [11]. Detailed structures of radial elements in Fig. 2d show several mineralized tesserae chains in each radial element and a higher mineralized area in the joints, and the location for the SEM and EDS studies.

3.2. Microstructure and composition

Micro-CT images of a representative midsection of the pectoral fin as well as single radial element are shown in Fig. 3. The average length of the radial elements is ~5.5 mm and the diameters vary from ~0.48 mm at the midsection to ~0.95 mm at the distal end. From Fig. 3a, it can be observed that the fin rays bifurcate into two branches ~2/3 of the length from the proximal region. From the dorsal view at a higher magnification (Fig. 3b), the proximal-distal position of the joints is not the same for each ray; the position mismatch of the nearest two joints in adjacent fin rays is ~1.2 mm. This joint position mismatch is thought to facilitate a variety of kinematic motions [8]. A cross section of a fin element (Fig. 3c) shows the dorsal and ventral components, but the dorsal tessera chain has two separate components, resulting in a 3-chain configuration. To the best of our knowledge, this is the first report of a 3-chain tesserae configuration. Each tessera has an average diameter ~100 μm. The mineral density increases from the outer surface to the inner core, indicating that softer tissues surround the higher mineralized core. This can be related to the backscatter scanning electron microscopy images of *Urobatis halleri*, which showed mineralized tesserae wrapped by unmineralized perichondrium [20]. As shown in Fig. 3d, the pectoral fins are bent at ~60°. This is accomplished by employing ~15 radial elements; only a ~4° orientation change between adjacent radial elements is necessary to achieve the large 60° angle.

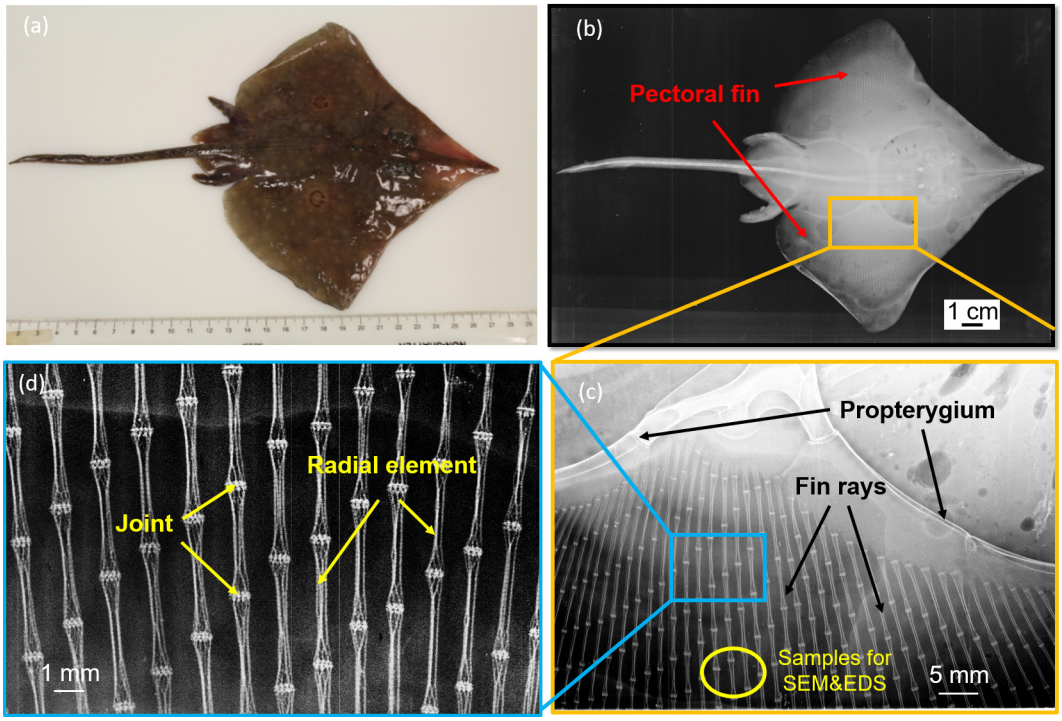

Fig. 2. The Longnose Skate skeleton and pectoral-fin structure: (a) Photograph of a fish collected along the San Diego coastline; (b) X-ray image of the whole skeleton; (c) Conjunction between the fin rays and the propterygium support element (orange box in (b)). Propterygium is indicated in the figure as the starting of fin rays. The fin rays are composed of radial elements separated by joints. The yellow circle shows the radial element samples used for scanning electron microscopy and electron dispersive X-ray spectroscopy analysis (Figs. 5, 6 and 7); (d) High magnification X-ray image of detailed radial elements and joints in the fin rays.

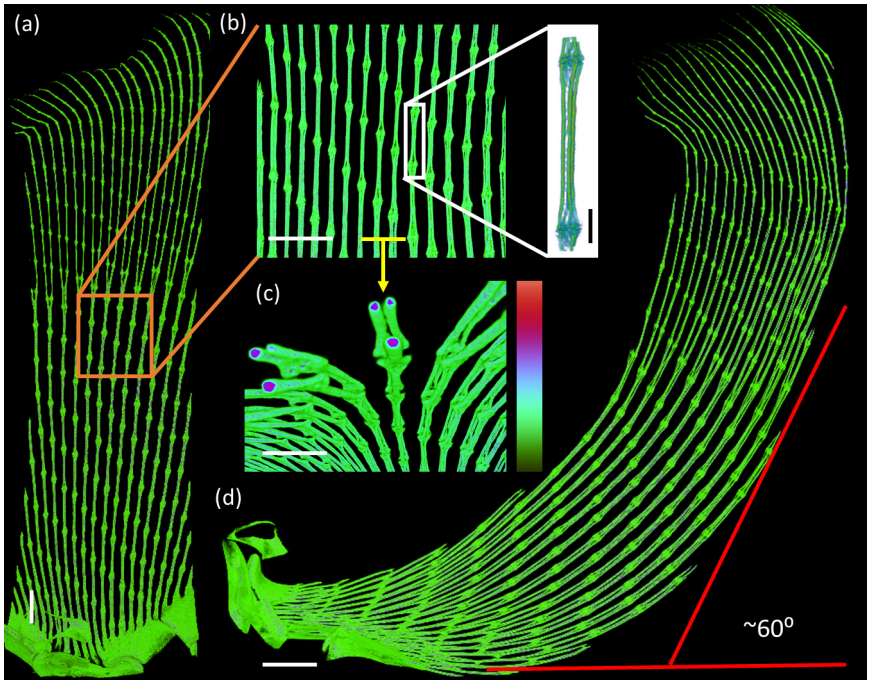

Fig. 3. Micro-computed tomography images of fin rays and radial elements: (a) Dorsal section of the left pectoral fin skeleton; (b) Dorsal view of radial elements and the joints between elements, single radial element is shown at a higher magnification; (c) Cross-section of radial element, showing three mineralized components in each element. The green color has a lower mineral density, the red color has a higher mineral density; (d) The pectoral fin bent ~60°, showing a gradually bending of each radial element. White scale bar (a) and (d): 5 mm, black scale bar (b): 1 mm.

From analysis of the μ-CT images (see Fig. 4 caption), the total area and percent of the mineralized tesserae in the cross section of five adjacent fin rays are plotted as a function of the distance from the proximal end of the fin rays (Fig. 4a). The purple strips in each fin ray indicate the 3-chain sections. The white areas between the purple strips are the highly mineralized ends of each

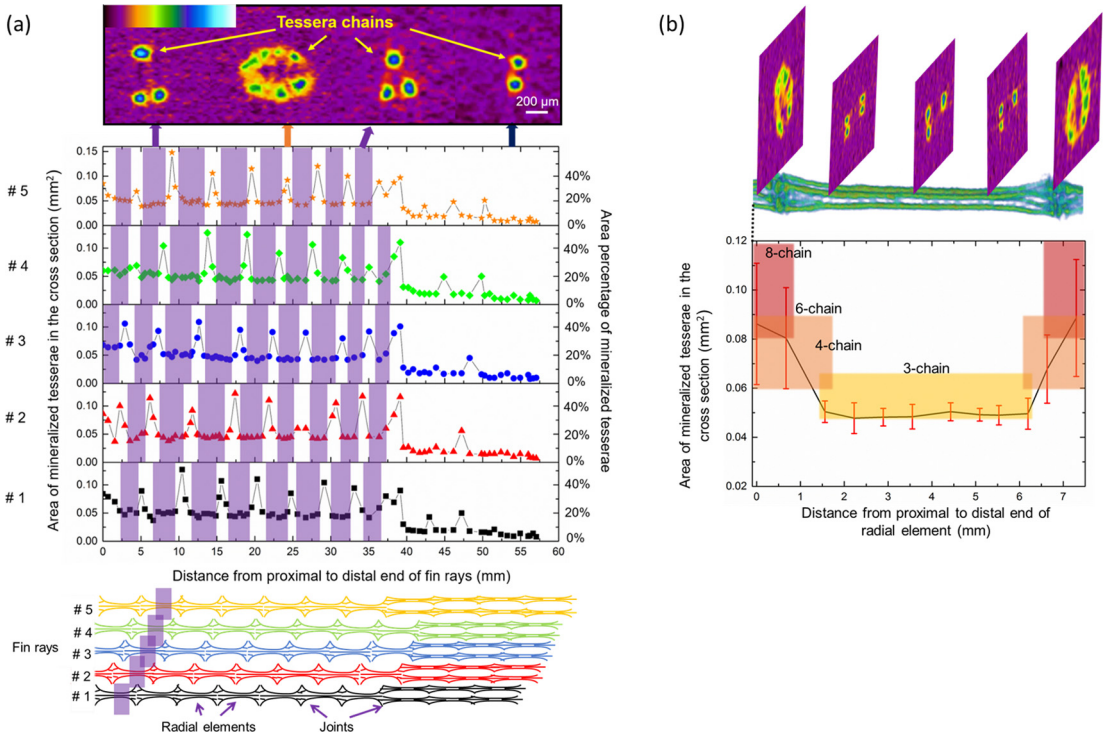

Fig. 4. Calcification patterns in fin rays and a single radial element: (a) (top) Cross-sectional micro-computed tomography images. Degree of mineralization increases from black (left) to white (right) in the color scale; (center) Plot of the area (left) and percentage (right) of mineralized tesserae in the cross section of five adjacent fin rays (bottom) as a function of distance from the proximal to distal end (unmineralized gaps in between two adjacent radial elements are not shown because of the relative small size). Areas of mineralized tesserae are calculated based on the area inside the yellow circles from the top cross-sectional micro-CT images. Total area of radial element cross section is determined by the largest cross section area in the joint part. Purple strips show the 3-chain sections in each fin ray, while the area between the purple strips are the highly mineralized ends of each radial element, which have six to eight chains. Cross-sectional μ-CT images are shown above the plots, illustrating the different number of tessera chains along the radial elements; (b) Plot of the area of mineralized tesserae and number of tesserae chains as a function of distance from proximal to distal end of a single radial element.

radial element, which have 6- to 8- chains, as shown in the accompanying micrograph. This corroborates results for other batoids, where highly mineralized regions with numerous chains are observed at the end of the radial elements [11]. There is a small gap containing unmineralized tissue in the joint between two radial elements, however it is too small to be shown on the length scale in Fig. 4. The highly mineralized ends (white strips) of each radial element represent the positions of joints, which shows a position mismatch of the adjacent five fin rays (indicated by the offset of the purple and white strips from #1 to #5). A large decrease in the mineralized area occurs ~40 mm from the proximal end because the radial elements merge. To obtain a better idea of how the mineralized area distributes within a single radial element, the average mineralization area as a function of the distance from proximal to distal end of a radial element is plotted in Fig. 4b. The mineralization area increases ~80% from the midsection of the radial element (3-chain), to the 4-chain region and finally to the 6–8 chain areas at the ends of each radial element. This indicates that the stiffness could significantly increase from the midsection to the proximal or distal end of each radial element. This may explain why the position mismatch of tesserae chains and joints in different fin rays is present, since the highly mineralized ends may function as a supporting point. Further studies on developing biomimetic structures can be based on insights gained from these analyses.

SEM and μ-CT images of radial element in different views are shown in Fig. 5. Fig. 5a shows a μ-CT image of a single ray element and joint from a dorsal-ventral view. A single slice micro-CT image was acquired from the central part of a radial element, showing the higher mineral density tesserae. Lateral view of radial elements from micro-CT image (Fig. 5b) indicates 3-chain tessera in each radial element. The ends of the radial elements are comprised of 6- to 8-chain tessera, indicating that the 3-chain configuration in the midsection of the radial element bifurcate, corroborating the results in Fig. 4b. The three circular cross sections of the tessera chains within one radial element can be identified in the micro-CT image (Fig. 5c). On the outer surface of each radial element is the perichondrium [14,18,29]. Detailed SEM images of the freeze-fractured cross section is presented in Fig. 5d. Three circular tesserae were found in the cross section of a radial element (Fig. 5d), further verifying the three chains shown in the micro-CT images. Aligned collagen fibers, with the periodic *d*-spacing of 67 nm, are observed in the perichondrium, wrapped around the tessera chains circumferentially (Fig. 5e), which has been observed by others [14,15]. EDS maps of Ca and P distribution in both longitudinal and cross sections are shown in Fig. 6. Ca and P are marked in the tesserae area in both views. The atomic ratio of Ca to P calculated from the EDS spectrum is ~1.21, which is less than the hydroxyapatite Ca/P found in shark skeletons (~1.5) [30,31] but within range found in teleost fish bones (1.20–1.68) [32]. Urist [31] found a lower Ca/P ratio ~1.52 in the spines of sharks and rays than the theoretical Ca/P value in hydroxyapatite (1.67), suggesting a biphasic calcium phosphate composition (a mixture of hydroxyapatite and β-tricalcium phosphate), in which there was ~75% hydroxyapatite. The low Ca/P ratio of tesserae found in present work may suggest that mineral present is biphasic calcium phosphate. In comparison, there is little or no Ca or P in the soft tissue and perichondrium.

Ultrastructural SEM and BSEM imaging of the cross- and longitudinal sections of a tessera were performed to further examine

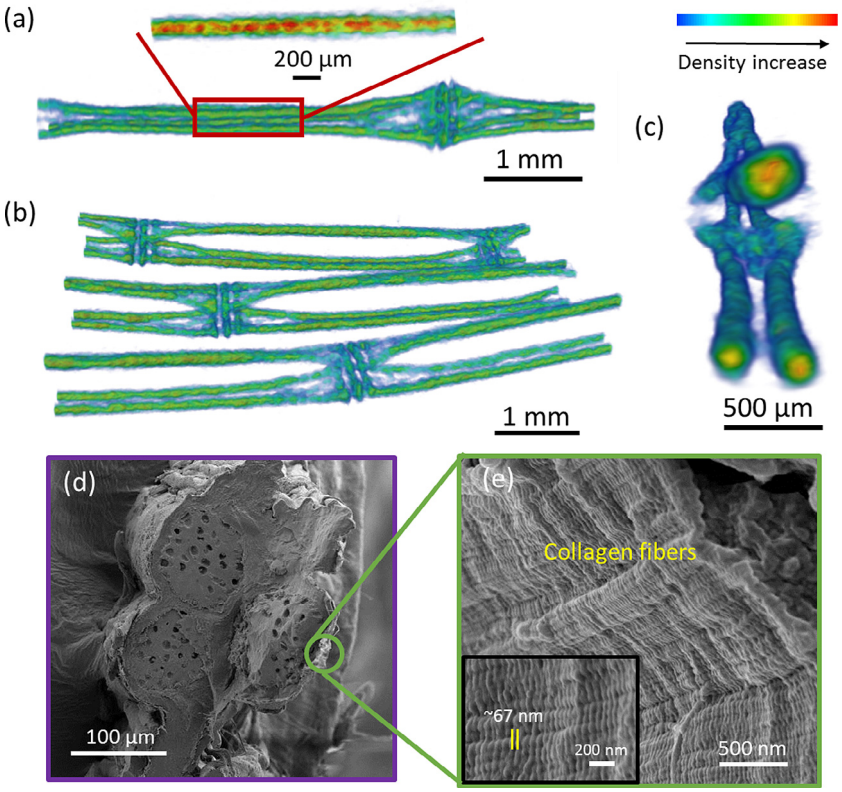

Fig. 5. Scanning electron microscopy and micro-computed tomography images of radial elements at different views. Images taken from the center of a radial element from the midsection of the pectoral fin: (a) Micro-computed tomography image of dorsal-ventral view of a radial element and the joint. Micro-computed tomography slice shows a series of discrete mineralized tesserae along the radial elements. The red color means higher mineral density corresponding to highly mineralized tesserae. The cartilage is in green, showing a lower mineral density; (b) Lateral view of radial elements and joints. Three tesserae chains in each radial element are shown; (c) Micro-computed tomography image of cross section of a radial element, showing three circular Mineralized tesserae and the surrounding unmineralized perichondrium soft tissue; (d) Microscopy image of cross section of a radial element. Three circular tesserae are observed; (e) Aligned collagen fibers are found in the outer layer of perichondrium that wrap around the tesserae.

the mineral distribution. The white circular area in a BSEM image (Fig. 7a) indicates that the tessera have a larger degree of mineralization. A high magnification image of a chondrocyte lacuna from a tessera shows fibrous network structure (Fig. 7b). No crystals are observed in the unmineralized tissue that surrounds the tessera (Fig. 7c). In contrast, a large number of mineralized nanoparticles are found in the tessera (Fig. 7d). Fig. 7e shows a BSEM image of the longitudinal section, indicating the discrete nature of highly mineralized tesserae chains and unmineralized tissue between intertesseral gaps. No crystals are found in the intertesseral gaps, but a fiber-like structure is observed (Fig. 7f), corroborating the results of Seidel et al. [20] who found collagen fibers bundles in the intertesseral gaps in the Round Stingray. Further studies are needed to identify the composition of the unmineralized tissues in these gaps in the Longnose Skate. These results further verify that the highest mineral density is within the tesserae and no minerals are found in the soft tissue surrounding and between them.

As a comparison to the SEM images, the longitudinal and cross section of the radial elements were stained with hematoxylin and eosin and observed with the optical microscope (Fig. 8). The discrete nature of tesserae is visible when Fig. 8a and b are compared; the former being a longitudinal optical microscopy section while the latter is a BSEM image. Muscle fibers are indicated in Fig. 8c surrounding the radial elements. The dark pink A-band and light pink I-band are comparable with the results in Fig. 5f, further demonstrating the existence of muscle fibers between the radial elements. A large number of chondrocytes occupy the joints between radial elements compared to the surrounding tissue (Fig. 8d). Three tesserae are observed in both the dorsal and ventral area in the cross section of the radial element near the joints (Fig. 8e). These six tesserae will eventually evolve into a 3-chain tessera (two in the dorsal and one in ventral) in the central part of the radial element, according to the structure observed in Fig. 3c and Fig. 4. Although tesseral spokes were observed in *Urobatis halleri* [20], we do not clearly observe them in the present images.

A schematic diagram of the hierarchical structure of the fin rays, compiled from the above structural results, is shown in Fig. 9. At the macro level (~1 mm), the fin rays are composed of ~15–20 end-to-end cartilaginous radial elements, which are separated by joints, forming a staggered pattern across the fin. At a micro level (~100 µm), the radial elements are composed of three parallel, chains of tesserae, which bifurcate at the radial ends to form 6- to 8-chains. These chains are formed by a series of discrete, cylindrical mineralized cartilaginous tissue. The tessera chains are embedded in an unmineralized cartilage matrix. In the longitudinal direction, the tesserae are separated by a gap of ~5 µm, which is filled with unmineralized tissue. Between adjacent fin rays are muscle fibers. At the nano level (~100 nm), collagen fibers are found in the perichondrium forming the outer layer of the radial elements.

3.3. Force analysis of undulation swimming

The fin elements can be considered as cantilever beams, and the stiffness of these beams directly affect the swimming efficiency

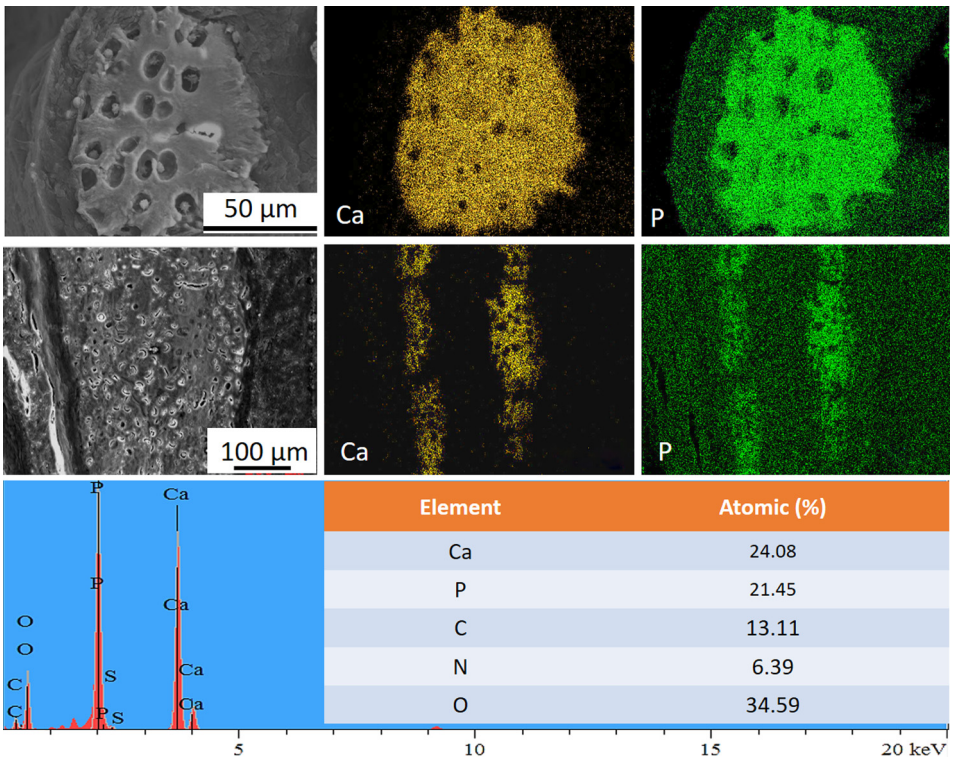

Fig. 6. Scanning electron microscopy images and electron dispersive X-ray spectroscopy (EDS) element maps and spectrum of the cross- and longitudinal sections of a radial element: Top: Cross-section of a tessera; Middle: Longitudinal section of a tessera series. Both show higher distribution of Ca and P in the tessera area, indicating a higher mineral density in the tesserae part; Bottom: EDS spectrum and elemental atomic concentration of a tessera.

[11]. From beam theory, the stiffness is determined by Young's modulus (E) and second moment of inertia (I). Since the batoid fishes need to keep their body as light as possible to keep buoyant because of the absence of a swim bladder, their cartilage skeleton helps to decrease their body weight [4,33]. However, this decrease in the Young's modulus leads to lower bending stiffness, which limits the efficient transmission of large forces during swimming. [34,35]. To solve this contradiction, a hierarchy was evolved to increase the stiffness of the whole fin skeleton using very few materials.

The bending force in the pectoral fin varies with time and position. Fig. 10 shows the force loading in the fin rays during undulatory swimming. The force can be divided into lift (y-axis) and thrust (x-axis) force, and the final combined forces vary in directions depending on the time and position during swimming [36]. As a result, the radial elements need to survive bending moments in all directions. From the μ-CT, SEM and histology images, it was demonstrated that the radial elements are composed of three mineralized tessera chains, two dorsal and one ventral, which is hypothesized to solve the problem of having forces applied in different directions. If a uniform load, q, is applied on a beam, the deflection δ is:

$$\delta = qL^4/8EI$$

where L is the average length. This equation can be applied to analysis of bending of the radial elements. A decrease in deflection can be realized by minimizing the length of radial elements or increasing E and/or I. Fig. A1 (Appendix I) is a schematic of the crustal, 2-chain, 3-chain and 4-chain calcification patterns. Following the previous analysis of Schaeffer and Summers [11], let A be equal to the overall cross-sectional area of a radial element and $A_{c_{total}}$ be equal to the total cross-sectional area of the mineralized tesserae, then the second moment of inertia in the lift direction (x is the neutral axis) and thrust direction (y is the neutral axis) are (see Appendix I for further details):

$$I_{x,crustal} = I_{y,crustal} = \frac{(2A - A_{c_{total}})A_{c_{total}}}{4\pi}$$

$$(A_{c_{total}} \leqslant A)$$

$$I_{x,2-chain} = \frac{(8A + 5A_{c_{total}} - 8\sqrt{2AA_{c_{total}}})}{8\pi}A_{c_{total}}; I_{y,2-chain} = \frac{A_{c_{total}}^2}{8\pi};$$

$$(A_{c_{total}} \leqslant 0.5A)$$

$$I_{x,3-chain} = I_{y,3-chain} = \frac{A_{c_{total}}^2}{12\pi} + \frac{A_{c_{total}}}{2}\left(\sqrt{\frac{A}{\pi}} - \sqrt{\frac{A_{c_{total}}}{3\pi}}\right)^2 = \frac{(3A_{c_{total}} + 6A - 4\sqrt{3AA_{c_{total}}})}{12\pi}A_{c_{total}}$$

$$(A_{c_{total}} \leqslant 0.66A)$$

$$I_{x,4-chain} = I_{y,4-chain} = \frac{(8A + 3A_{c_{total}} - 8\sqrt{AA_{c_{total}}})}{16\pi}A_{c_{total}}$$

$$(A_{c_{total}} \leqslant 0.68A)$$

By calculating the I for the different formations, it is found that there is a limitation to A_c for each pattern. For the crustal pattern, the maximum calcification area, $A_{c_{total}}$, can be equal to A. While in the other patterns, A_c is limited by geometry. The largest I_x in each tessellated pattern can be calculated: $I_{x,crustal} = 0.25A^2/\pi$, $I_{x,2-chain} = 0.16A^2/\pi$, $I_{y,3-chain} = 0.13A^2/\pi$, $I_{x,4-chain} = 0.15A^2/\pi$. By

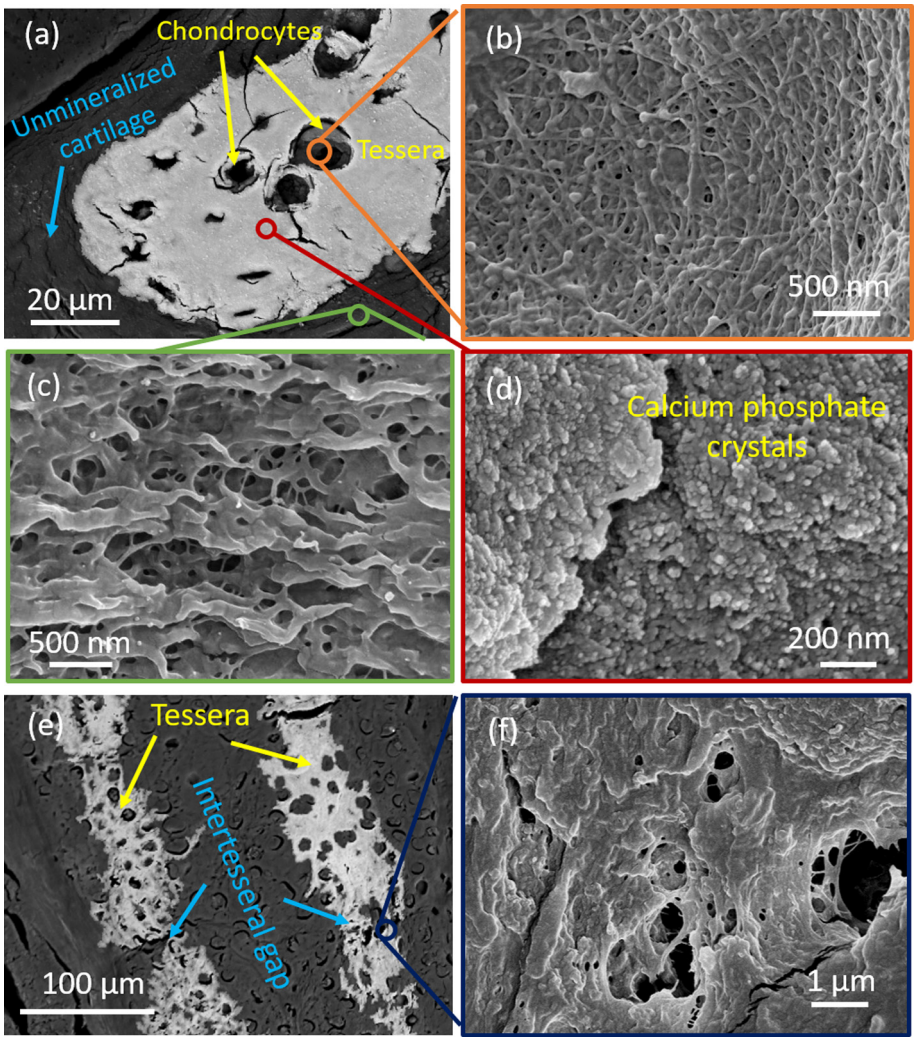

Fig. 7. Ultrastructural scanning electron microscopy and backscattering scanning electron microscopy images of the cross- and longitudinal sections of a single radial element: (a) Backscattering scanning electron microscopy image of the cross-section showing the tesserae and unmineralized cartilage surrounding the tesserae; (b) Structure inside a chondrocyte lacuna at a higher magnification; (c) Ultrastructure of unmineralized cartilage surrounding the tesserae; (d) Calcium phosphate crystals in the mineralized tessera; (e) Backscattering scanning electron microscopy image of longitudinal section showing tesserae (white) and the intertesseral gap between adjacent tessera; (f) Unmineralized tissue in the intertesseral gap.

keeping the calcification area $A_{c_{total}} = 0.5A$ as a constant, the I_x values for different patterns can be compared: $I_{x,crustal} = 0.19A^2/\pi$, $I_{x,2-chain} = 0.16A^2/\pi$, $I_{x,3-chain} = 0.11A^2/\pi$, $I_{x,4-chain} = 0.12A^2/\pi$. I_x in crustal pattern is the largest, while it is smaller for the 2-, 3- and 4-chain configurations. From the perspective of obtaining the highest stiffness, the crustal configuration is the best. The bending force does not just come only from dorsoventral (y-axis) motion, thus the x-axis is not always the neutral axis. The maximum I_y in the perpendicular direction with y as the neutral axis, $I_{y,crustal} = 0.19/\pi$, $I_{y,2-chain} = 0.03A^2/\pi$,$I_{y,3-chain} = 0.11A^2/\pi$, $I_{y,4-chain} = 0.12A^2/\pi$. For the 2-chain structure, once the bending force changes from thrust to lift, the neutral axis changes from the x- to the y-axis, it was previously found that I decreases ~80% [11], which is comparable with the present results. This dramatic decrease of stiffness along the y-axis makes it harder to support the thrust force in this direction. Although the crustal calcification pattern provides the highest stiffness in all force directions, the 3- and 4-chain patterns allow for angle-independent stiffness with better flexibility. In the present work, μ-CT and SEM images show the pectoral fins of the Longnose Skate have a 3-chain structure, indicating its pectoral fins can withstand force from various angles.

3.4. Mechanical implication of the tesserae structure

Tesserae structures have long been considered as a design to increase the resistance to fatigue damage as well as extreme bending [23]. A schematic of the cross section of a 2-chain radial element is employed to explain the stress distribution using a cantilever beam model under a uniform load q (Fig. 11a). In the schematic diagram, sandwich beam theory is applied [37]. In the core is the unmineralized cartilage with a low Young's modulus. Surrounding this are the highly mineralized tessera chains with higher Young's modulus. According to the Euler-Bernoulli theory, the axial strain ($\varepsilon_{xx}(x,z)$) and stress ($\sigma_{xx}(x,z)$) can be calculated as:

$$\varepsilon_{xx}(x,z) = -z\frac{d^2w}{dx^2}$$

$$\sigma_{xx}(x,z) = -zE(z)\frac{d^2w}{dx^2}$$

where w represents the deflection and $E(z)$ is the Young's modulus. The bending moment and shear force is then given by:

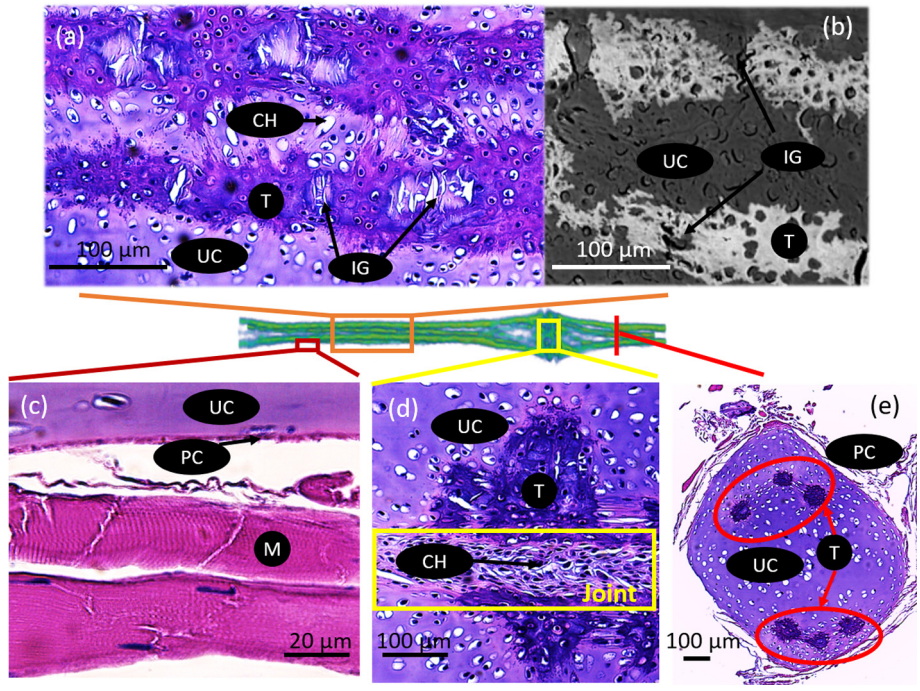

Fig. 8. Optical microscopy images of hematoxylin and eosin stained fin radial element sections. (a) Longitudinal cross section where chondrocytes (CH, white areas), calcified cartilage tesserae (T, dark purple) and unmineralized cartilage (UC, light purple) are indicated. Unmineralized tissue is shown in the gap between the tesserae (IG, intertesseral gap). (b) Backscattering scanning electron microscopy image of a longitudinal section as a comparison, showing the discrete mineralized tesserae (white) and intertesseral gaps. (c) Muscle fibers (M) on the outer layer of the radial element. Dark pink color of A band and light pink of I band are shown. The perichondrium (PC) is shown sandwiched between the cartilage and muscle fibers. (d) Chondrocytes in the joint between two adjacent radial elements. (e) Cross section of a single radial element near the joint. Dorsal and ventral tesserae are indicated in dark purple color.

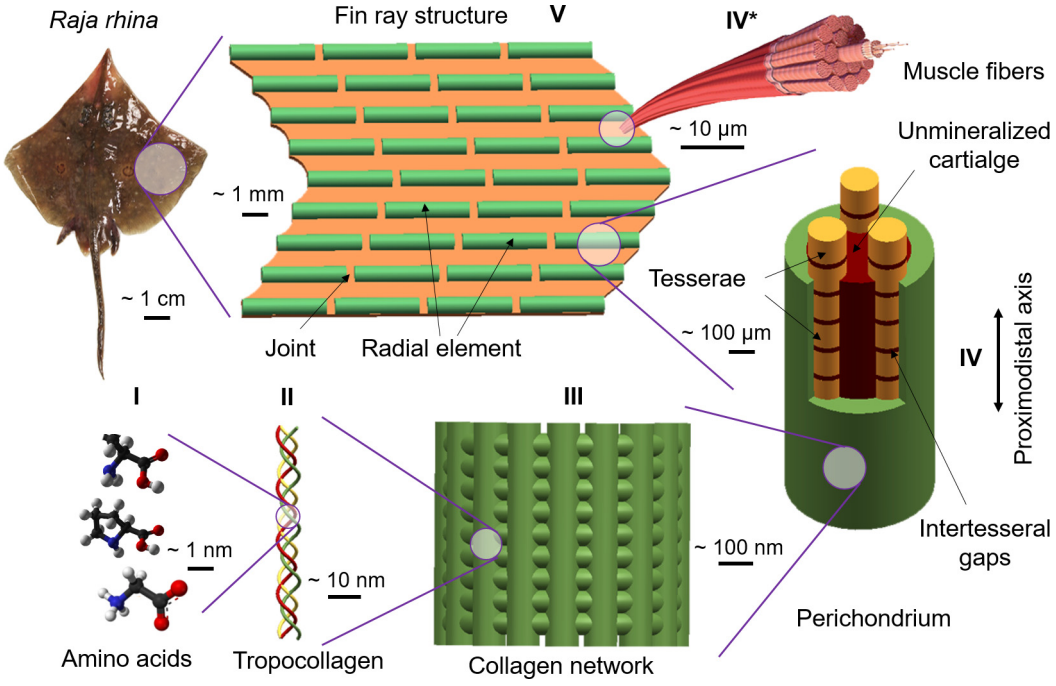

Fig. 9. Hierarchical structure of the pectoral fin in the Longnose Skate (*Raja rhina*): Level I: amino acids, which are the basic components of collagen; level II: tropocollagen; level III: collagen network in the perichondrium; level IV: radial element, which is composed of a series of three mineralized tesserae (yellow), which are sounding by soft perichondrium (green). Between the tesserae is unmineralized cartilage (red); level IV*: muscle fibers are found between radial elements; level V: pectoral fin consists of several finger like fin rays, and each fin ray has end-to-end connected radial elements.

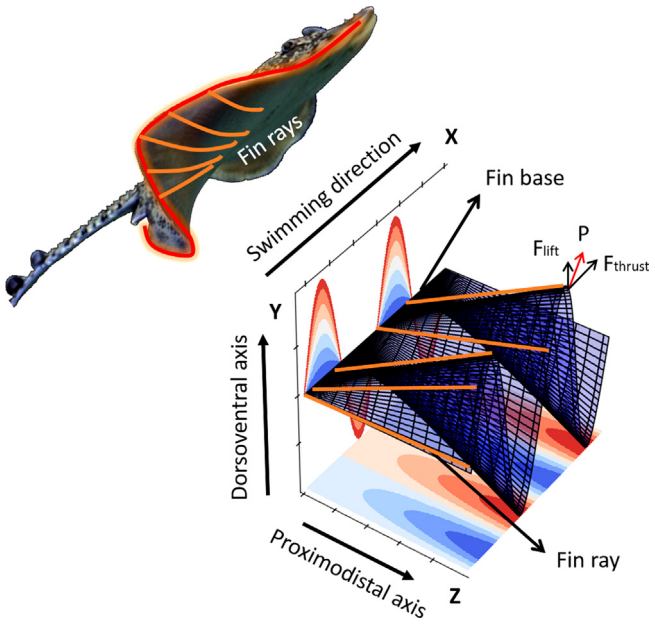

Fig. 10. Force analysis in undulation swimming: schematic of pectoral fin in undulation swimming. *X* is the swimming direction, pectoral fin forms a sine wave-like shape during undulation, the force on a single fin ray can be divided into lift force and thrust force, and the final force is perpendicular to the fin surface with is marked as *P*. *P* can be in various directions as the time and position of fin rays change.

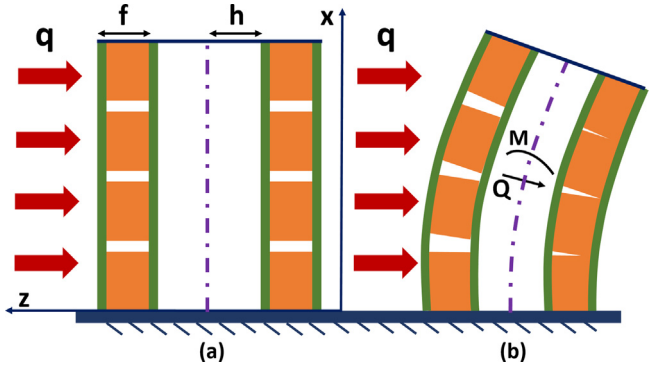

Fig. 11. Schematic diagram of sandwich model of a 2-chain structure during bending: (a) Longitudinal section of a radial element before applying uniform force q and (b) bending results showing how the discrete cylindrical tesserae deform under tension and compression. Orange areas are the discrete tesserae and the green line is the soft tissue (collagen) that wraps the tesserae. The white regions are the soft unmineralized cartilage. The purple dotted line is the neutral axis. f = tesserae thickness, 2 h = thickness of unmineralized cartilage. Q = shear force and M = bending moment.

$$M_x(x) = \int\int^{z} \sigma_{xx} dz dy = -D\frac{d^2w}{dx^2}$$

$$D = \int\int z^2 E(z) dz dy$$

$$Q_x = \frac{dM_x}{dx}$$

where D is the flexural stiffness of the beam, M_x is the bending moment, Q_x is the shearing force. For a sandwich structure of unit width (y-direction) with a $2h$ (~1 mm) thick core (unmineralized cartilage core), and two face materials (mineralized tesserae) with thickness f (~100 μm) with the Young's modulus of unmineralized cartilage core and tesserae face materials E_c and E_f, respectively. The axial and shear stresses in the beam are (assuming that $E_f \gg E_c$ and $f \ll 2h$):

$$\sigma_{xx}^f \approx \mp\frac{M_x}{2fh};\ \sigma_{xx}^c \approx 0$$

$$\tau_{xz}^f \approx 0;\ \tau_{xz}^c \approx \frac{Q_x}{2h}$$

where σ_{xx}^f and σ_{xx}^c are the axial stresses on the face and core material respectively and τ_{xz}^f and τ_{xz}^c are the shear stresses on the tesserae face and unmineralized cartilage core, respectively. It can be concluded that the axial forces are carried by the tessera series, while the shear stresses are taken by the unmineralized cartilage core [38]. As a result, under bending, the main stresses on the mineralized tessera series are subjected to uniaxial tensile or compressive stress. The discrete nature of the tessera structure with unmineralized cartilage between each tessera makes it possible to sustain large tensile strains, as shown in Fig. 11b.

Fig. 12 shows single fin element tensile test stress-strain curve, which shows similar tensile behavior of other biopolymers such as collagen, presenting a *J*-shaped curve. This is reasonable because of the mineralized tesserae are discrete and the load is mainly carried by the organic material present in the intertesseral joint. This is supported by the large maximum strain of ~15–20%, which is not achievable in a ceramic phase. The maximum strain here is comparable with the pure cartilage in hagfish [39]. The ultimate strength is ~5 MPa, the ultimate strain is ~0.20 and the Young's modulus is ~20 MPa. This is comparable to the compressive strength, ultimate strain and stiffness of vertebrate in a Torpedo Ray (4.5 MPa, 0.22 and 25.5 MPa, respectively), a batoid fish [40], as shown in Table 1. Russo et al. [8] examined the tensile response of cartilage extracted from Cownose and Atlantic Rays. The stress-strain curves were not reported, only the fracture strain of ~0.15, which corroborated the present result. The mineralized cartilage vertebrae in Sand Tiger Sharks have compressive strength, ultimate strain and stiffness of 16 MPa, 0.14 and 167 MPa, respectively [41], similar to values found in vertebrae and hyomandibular cartilage in Smooth-hound sharks [42,43]. In comparison, the elastic modulus of lamprey annular cartilage (unmineralized) ranged from 0.71 to 4.85 MPa, while cartilage from bovine ears (unmineralized) was around 1.94 MPa [44]. The reason of this ten fold increase of the Young's modulus reported here in mineralized cartilage over unmineralized cartilage can be attributed to the presence of a mineral phase.

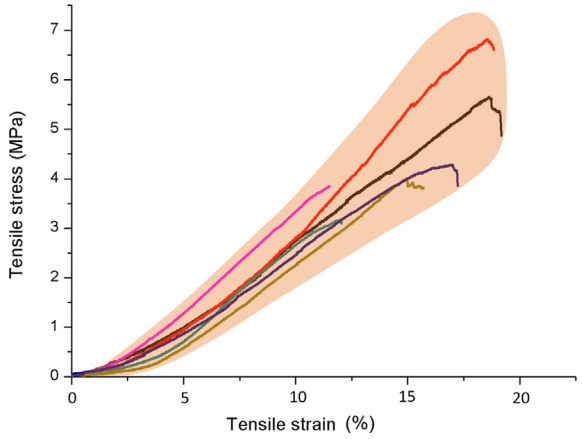

Fig. 12. Tensile stress-strain curves for a single radial element under quasi-static uniaxial loading.

Table 1
Comparison of mechanical properties of mineralized and non-mineralized cartilage tissues.

	Elastic modulus (MPa)	Tensile strength (MPa)	Compressive strength (MPa)	Ultimate strain (%)	Refs.
Longnose Skate fin	20	5		15–20	
Torpedo Ray vertebrate	25.5		4.5	22	[41]
Sand Tiger Shark vertebrate	167		16	14	[42]
Lamprey eel annular cartilage	0.71–4.85				[45]
Bovine ears	1.94				[45]

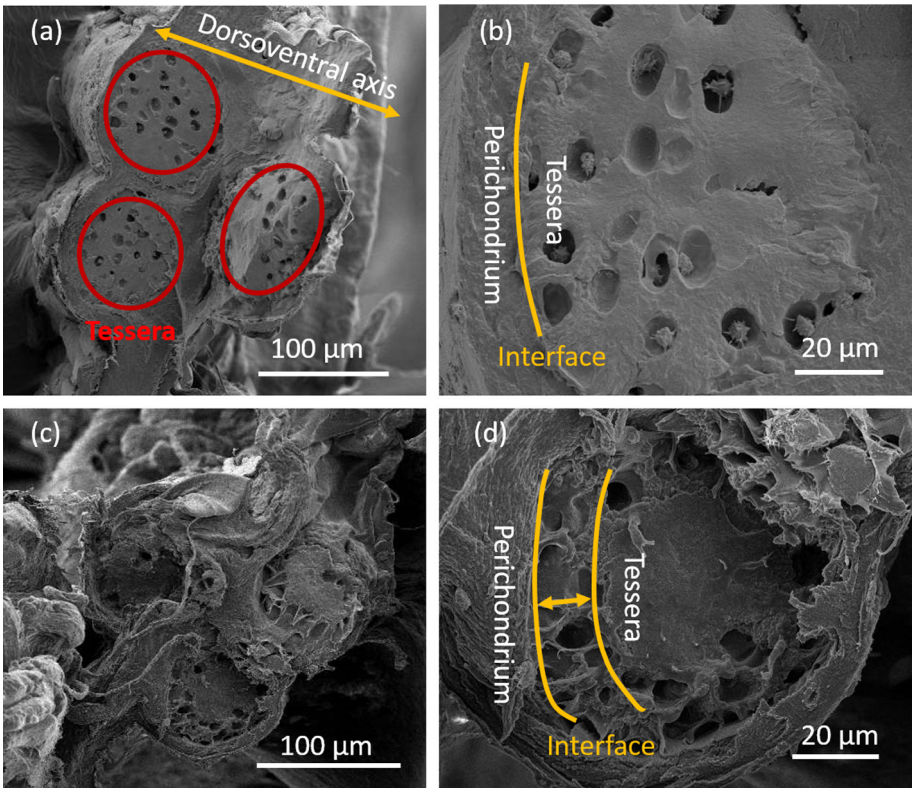

Fig. 13. Scanning electron microscopy images of tensile fracture cross-sectional surfaces. Freeze-fractured sample: (a) Red circles are the three tesserae and (b) higher magnification image shows a tessera and perichondrium interface. Ambient condition sample: (c) Unmineralized perichondrium and tessera become unattached with each other and (d) higher magnification image shows the enlarged gap area in the interface compared to the thin layer interface before tension, shown in (b).

Fig. 13a and b shows SEM micrographs of the fracture surface after tensile freeze-fracturing. The surfaces are smooth and it is difficult to locate the failure point. After tensile fracture under ambient conditions, the outer surface soft tissue layer became unattached to the tessera, caused by the stress on the soft tissue (Fig. 13c). The interface between tessera and its surrounding perichondrium (Fig. 13b) was damaged, showing an enlarged interface opening compared to the original tightly adhered interface (Fig. 13d). Under uniaxial tensile loading, a larger displacement occurs in the soft perichondrium layer and in the unmineralized gaps between the tesserae, while less displacement occurs in the mineralized tesserae. This mismatch of Young's modulus and displacements could possibly cause the interface damage. By combining two different materials, the soft tissues that can extend under tensile loading and hard tissues for sustaining compressive loading, this structural design successfully uses the materials to reach more optimal stiffness for both tensile and compressive loading [23,25].

4. Conclusions

The hierarchical structure of the pectoral fins from a representative batoid fish – the Longnose Skate (*Raja rhina*), from the macro to nano scale was studied. Scanning electron and optical microscopy and micro-computed tomography were used to examine and quantify the micro- to macro-structural organization. Tensile tests and structural analysis of the fin ray elements were used to explain the configuration of the mineralized regions in the fin rays. The major findings are:

- The whole pectoral fin is composed of ~70 finger-like fin rays, and each fin ray consists of 15–20 radial elements separated by joints. The radial elements have are ~5.5 mm long with diameters ranging between ~0.5 and 1.0 mm.
- Each radial element has three parallel, mineralized cylindrical tessera chains, ~100 μm in length and ~80 μm in diameter. This is the first report of a 3-chain tesserae configuration.
- The 3-chain tesserae exist in the middle of each radial element, while six to eight highly mineralized chains exist at the two ends. There is a 1–2 mm mismatch of the joint position between two adjacent fin rays. A large decrease in the mineralized area occurs ~40 mm from the proximal end because of the bifurcation of radial elements.
- Each tessera chain consists of a series of mineralized (calcium phosphates) cartilage embedded in unmineralized cartilage, forming the radial elements. These elements are wrapped by

circumferentially by aligned collagen fibers. Between the tesserae in the longitudinal direction there is a gap of ~5 μm, which is filled with unmineralized tissue. Between the radial elements, muscle fibers are found that likely control the movement of the radial elements.

- The second moments of inertia were calculated based on the different mineralized pattern: crustal, 2-chain, 3-chain and 4-chain. The newly observed 3-chain structure shows angle-independent stiffness and a higher stiffness than the 2-chain structure in supporting both lift and thrust forces.
- Tensile tests on single radial element illustrate a large maximum strain of ~20%, which is attributed to deformation of the unmineralized tissues as well as the damage of the interface between soft perichondrium and hard tesserae.
- A 2D analysis of bending deformation shows that the softer collagen can support large shear stresses and the gaps between mineralized tesserae in the radial elements can expand or compress to support tensile or compressive loads, thereby increasing the flexibility of the fin.

In summary, the hierarchical structure of the Longnose Skate pectoral fin ray, which is a composite of chains of discrete mineralized cartilage tesserae embedded in a soft matrix, has implications for the mechanical design of strong but flexible structural materials.

Acknowledgements

This research was funded by a Multi-University Research Initiative through the Air Force Office of Scientific Research (AFOSR-FA9550-15-1-0009) and a by a National Science Foundation, Division of Materials Research, Biomaterials Program Grant 1507169.

Appendix I. Calculation of second moments of inertia

Fig. A1 shows the configurations of the crustal, 2-chain, 3-chain and 4-chain catenated structures used for the analysis. The geometrical analysis for the calculations is expanded on the previous results of Schaefer and Summers [11].

The calculations are based on the parallel axis theorem. The second moment of inertia of circle with radius R:

$$I_x = I_y = \frac{\pi}{4}R^4$$

In the above analysis, R = outer radius of a fin ray element (green outline), r = radius of mineralized cylindrical block. Assuming an arbitrary neutral axis m, the second moment of inertia with respect to the m axis in different calcification pattern is:

(a) Crustal

$$I_{m,crustal} = \frac{\pi}{4}(R^4 - r^4)$$

$$R^4 = \left(\frac{A}{\pi}\right)^2;\ r^4 = \left(\frac{A - A_{c_{total}}}{\pi}\right)^2$$

$$I_{m,crustal} = \frac{\pi}{4}\left[\left(\frac{A}{\pi}\right)^2 - \left(\frac{A - A_{c_{total}}}{\pi}\right)^2\right] = \frac{(2A - A_{c_{total}})\cdot A_{c_{total}}}{4\pi}$$

$$r < R;\ A_{c_{total}} < A$$

The result is independent of θ, which means that the second areal moment of this configuration is the same for any centroidal direction.

(b) 2-chain catenated

$$A = \pi R^2;\ A_{c_{total}} = 2 \times \pi r^2$$

$$I_{m,2-chain} = 2 \times \left\{\frac{\pi}{4}r^4 + \pi r^2[(R-r)sin\theta]^2\right\}$$

$$I_{m,2-chain} = \frac{\pi}{2}\left(\frac{A_{c_{total}}}{2\pi}\right)^2 + A_{c_{total}}\left(\sqrt{\frac{A}{\pi}} - \sqrt{\frac{A_{c_{total}}}{2\pi}}\right)^2 sin^2\theta = \frac{\left[A_{c_{total}} + 8\left(A + 0.5A_{c_{total}} - \sqrt{2AA_{c_{total}}}\right)sin^2\theta\right]}{8\pi}A_{c_{total}}$$

$$r \leqslant 0.5R;\ A_{c_{total}} \leqslant 0.5A$$

(c) 3-chain catenated

$$I_{m,3-chain} = 3 \times \frac{\pi}{4}r^4 + \pi r^2\left\{[(R-r)sin\theta]^2 + \left[(R-r)\sin\left(\frac{\pi}{3} - \theta\right)\right]^2 + \left[(R-r)\sin\left(\frac{\pi}{3} + \theta\right)\right]^2\right\} = \frac{3}{4}\pi r^4 + \pi r^2(R-r)^2 \times \left\{\frac{3}{2} - \frac{1}{2}\left[cos2\theta + \cos\left(\frac{2\pi}{3} - 2\theta\right) + \cos\left(\frac{2\pi}{3} + 2\theta\right)\right]\right\} = \frac{3}{4}\pi r^4 + \pi r^2(R-r)^2 \times \frac{3}{2} = \frac{3}{4}\pi r^4 + \frac{3}{2}\pi r^2(R-r)^2$$

The result is independent of θ, which means that the second areal moment of this configuration is the same for any centroidal direction.

$$A = \pi R^2;\ A_{c_{total}} = 3 \times \pi r^2$$

$$I_{m,3-chain} = \frac{3\pi}{4}\left(\frac{A_{c_{total}}}{3\pi}\right)^2 + \frac{3}{2}\pi \times \frac{A_{c_{total}}}{3\pi} \times (R-r)^2 = \frac{(6A + 3A_{c_{total}} - 4\sqrt{3AA_{c_{total}}})}{12\pi}A_{c_{total}}$$

$$r \leqslant 0.46R;\ A_{c_{total}} \leqslant 0.65A$$

(d) 4-chain catenated

$$A = \pi R^2;\ A_{c_{total}} = 4 \times \pi r^2$$

$$I_{m,4-chain} = 4 \times \frac{\pi}{4}r^4 + 2\pi r^2(R-r)^2(sin^2\theta + cos^2\theta) = 4 \times \frac{\pi}{4}r^4 + 2\pi r^2(R-r)^2 = \pi\left(\frac{A_{c_{total}}}{4\pi}\right)^2 + 2\pi\left(\frac{A_{c_{total}}}{4\pi}\right)\left(\sqrt{\frac{A}{\pi}} - \sqrt{\frac{A_{c_{total}}}{4\pi}}\right)^2 = \frac{(8A + 3A_{c_{total}} - 8\sqrt{AA_{c_{total}}})}{16\pi}A_{c_{total}}$$

$$r \leqslant 0.41R;\ A_{c_{total}} \leqslant 0.68A$$

The result is independent of θ, which means that the second areal moment of this configuration is the same for any centroidal direction.

The second moment of inertia (I_m) as a function of the neutral axis angle θ in different calcification patterns is plotted in Fig. A2, indicating I_m is independent with angle in crustal, 3-chain and 4-chain patterns, but significantly changes for the 2-chain pattern. This plot is for $A_c/A = 0.5$, which is the maximum value for the 2-chain pattern.

However, from the above equations, the second moment of inertia (I_m) depends on the calcification area A_c. A plot of I_m as a function of the calcification area (A_c/A) is shown in Fig. A3. The second moment of inertia increases with calcification area in all patterns. Since the actual calcification area in fin radial elements

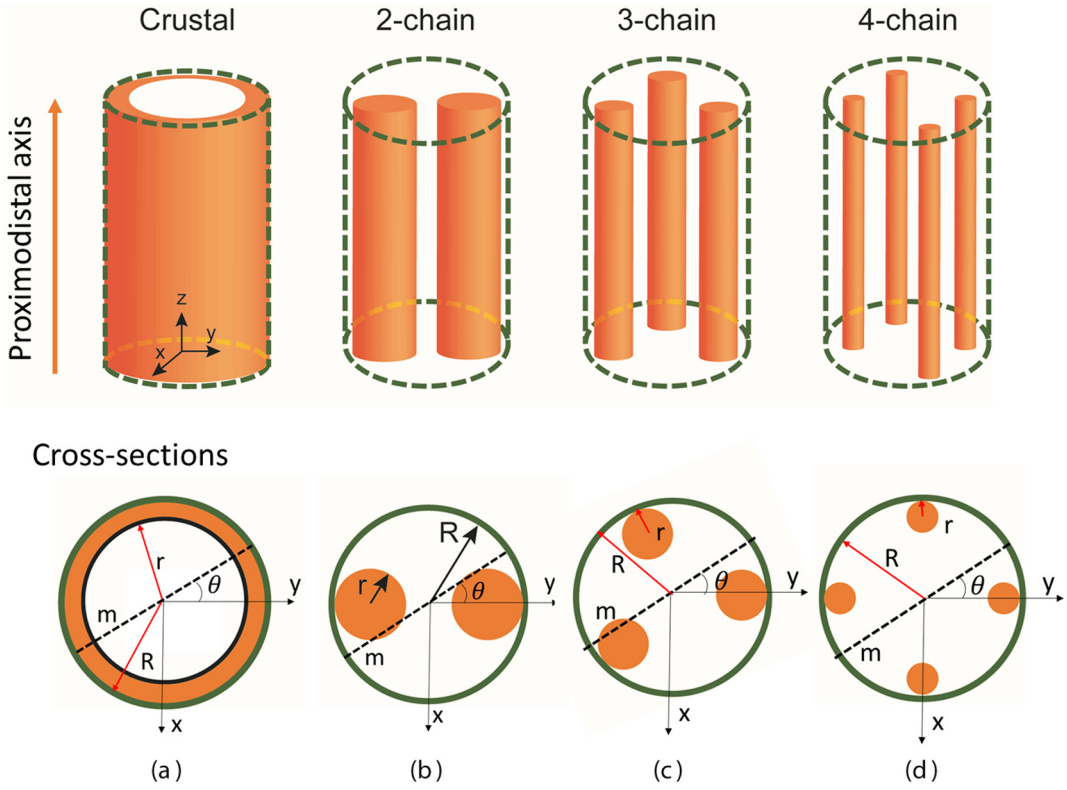

Fig. A1. Schematic diagrams of the radial element in a fin ray. Total cross section area A (indicated by green outline) and mineralized cross-section area A_c (orange cylinders) for (a) crustal, (b) 2-chain, (c) 3-chain and (d) 4-chain catenated. The white areas are unmineralized cartilage and the orange areas are mineralized tesserae. The axis 'm' is an arbitrary axis.

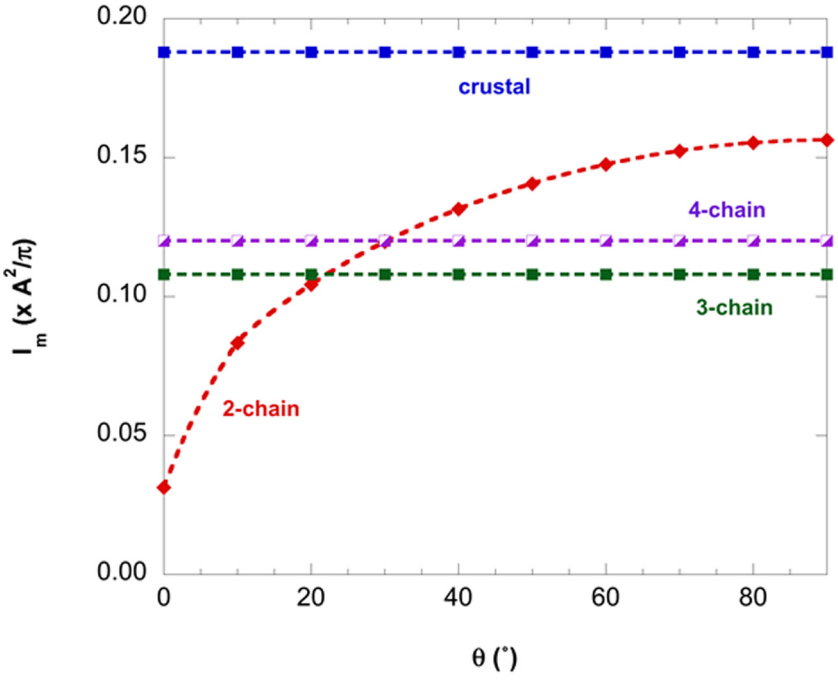

Fig. A2. Second moment of inertia (I_m) as a function of the neutral axis angle θ in different calcification patterns (crustal, 2-chain, 3-chain and 4-chain).

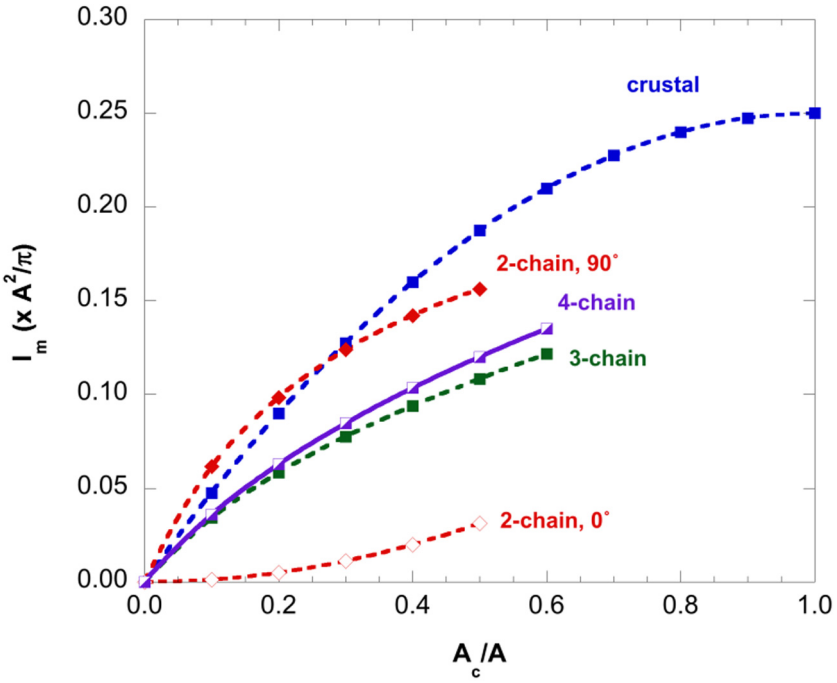

Fig. A3. Second moment of inertia (I_m) as a function calcification area (A_c/A) in different calcification patterns (crustal, 2-chain, 3-chain and 4-chain). Since I_m depends on the neutral axis angle in 2-chain pattern, I_m is plotted when $\theta = 0°$ and 90°, which is the lower and upper limit, respectively.

changes with position in the pectoral fin, this plot can provide a better understanding of how the I_m is not only a function of the chain pattern, but also of the calcification area.

References

[1] A.P. Farrell, E.D. Stevens, J.J. Cech, J.G. Richards, Encyclopedia of Fish Physiology: From Genome to Environment, Academic Press, an imprint of Elsevier, London; Waltham, MA, 2011.
[2] J.J. Videler, Fish Swimming, 1st ed., Chapman & Hall, London; New York, 1993.
[3] S. Alben, P.G. Madden, G.V. Lauder, The mechanics of active fin-shape control in ray-finned fishes, J. R. Soc. Interface 4 (13) (2007) 243–256.
[4] G.S. Helfman, B.B. Collette, D.E. Facey, B.W. Bowen, The Diversity of Fishes: Biology, Evolution, and Ecology, 2nd ed., Wiley-Blackwell, Chichester, UK, 2009.
[5] M. Sfakiotakis, D.M. Lane, J.B.C. Davies, Review of fish swimming modes for aquatic locomotion, IEEE J. Oceanic Eng. 24 (2) (1999) 237–252.
[6] L.J. Rosenberger, Pectoral fin locomotion in batoid fishes: Undulation versus oscillation, J. Exp. Biol. 204 (2) (2001) 379–394.
[7] G.V. Lauder, Fish locomotion: Recent advances and new directions, Annu. Rev. Mar. Sci. 7 (2015) 521–545.
[8] R.S. Russo, S.S. Blemker, F.E. Fish, H. Bart-Smith, Biomechanical model of batoid (skates and rays) pectoral fins predicts the influence of skeletal structure on fin kinematics: Implications for bio-inspired design, Bioinspiration Biomimetics 10 (4) (2015) 046002.
[9] S.-J. Park, M. Gazzola, K.S. Park, S. Park, V. Di Santo, E.L. Blevins, J.U. Lind, P.H. Campbell, S. Dauth, A.K. Capulli, Phototactic guidance of a tissue-engineered soft-robotic ray, Science 353 (6295) (2016) 158–162.
[10] H. Ehrlich, Biological Materials of Marine Origin, Springer, New York, 2013.
[11] J.T. Schaefer, A.P. Summers, Batoid wing skeletal structure: Novel morphologies, mechanical implications, and phylogenetic patterns, J. Morphol. 264 (3) (2005) 298–313.
[12] T. Ørvig, Histologic studies of placotlerms and fossil elasmobranchs. I. The endoskeleton, with remarks on the hard tissues of lower vertebrates in general, Ark. Zoologi 2 (1951) 321–454.
[13] S.P. Applegate, A survey of shark hard parts, in: P.W. Gilbert, R.T. Mathewson, D.P. Rall (Eds.), Sharks, Skates and Rays, The Johns Hopkins Press, Baltimore, MD, 1967, pp. 37–67.
[14] N.E. Kemp, S.K. Westrin, Ultrastructure of calcified cartilage in the endoskeletal tesserae of sharks, J. Morphol. 160 (1) (1979) 75.
[15] M.L. Moss, Skeletal tissues in sharks, Am. Zool. 17 (2) (1977) 335–342.
[16] J. Clement, Re-examination of the fine structure of endoskeletal mineralization in Chondrichthyans: Implications for growth, ageing and calcium Homeostasis, Mar. Freshwater Res. 43 (1) (1992) 157–181.
[17] M. Egerbacher, M. Helmreich, E. Mayrhofer, P. Böck, Mineralisation of the hyaline cartilage in the small-spotted dogfish *Scyliorhinus canicula* L, Scripta Medica (BRNO) 79 (2006) 199–212.
[18] M.N. Dean, C.G. Mull, S.N. Gorb, A.P. Summers, Ontogeny of the tessellated skeleton: insight from the skeletal growth of the round stingray *Urobatis halleri*, J. Anat. 215 (3) (2009) 227–239.
[19] J.G. Maisey, The diversity of tessellated calcification in modern and extinct chondrichthyans, Rev. Paléobiol. 32 (2013) 355–371.
[20] R. Seidel, K. Lyons, M. Blumer, P. Zaslansky, P. Fratzl, J.C. Weaver, M.N. Dean, Ultrastructural and developmental features of the tessellated endoskeleton of elasmobranchs (sharks and rays), J. Anat. 229 (2016) 681–702.
[21] D.O. Wagner, P. Aspenberg, Where did bone come from? An overview of its evolution, Acta Orthopaedica 82 (4) (2011) 393–398.
[22] M.I. Coates, S.E.K. Sequeira, I.J. Sansom, M.M. Smith, Spines and tissues of ancient sharks, Nature 396 (6713) (1998) 729–730.
[23] X.X. Liu, M.N. Dean, A.P. Summers, J.C. Earthman, Composite model of the shark's skeleton in bending: A novel architecture for biomimetic design of functional compression bias, Mater. Sci. Eng., C 30 (8) (2010) 1077–1084.
[24] X.X. Liu, M.N. Dean, H. Youssefpour, A.P. Summers, J.C. Earthman, Stress relaxation behavior of tessellated cartilage from the jaws of blue sharks, J. Mech. Behav. Biomed. Mater. 29 (2014) 68–80.
[25] P. Fratzl, O. Kolednik, F.D. Fischer, M.N. Dean, The mechanics of tessellations – bioinspired strategies for fracture resistance, Chem. Soc. Rev. 45 (2) (2016) 252–267.
[26] M.N. Dean, A.P. Summers, Mineralized cartilage in the skeleton of chondrichthyan fishes, Zoology 109 (2006) 164–168.
[27] M.N. Dean, S.N. Gorb, A.P. Summers, A cryoSEM method for presservation and visualization of calcified shark cartilage (and other stubborn heterogeneous skeletal tissues), Microsc. Today 16 (2008) 48–50.
[28] S. Mulvaney, P.J. Motta, The morphology of the cephalic lobes and anterior pectoral fins in six species of batoids, J. Morphol. 274 (2014) 1070–1083.
[29] M.A. Kolmann, D.R. Huber, M.N. Dean, R.D. Grubbs, Myological variability in a decoupled skeletal system: Batoid cranial anatomy, J. Morphol. 275 (8) (2014) 862–881.
[30] M.N. Dean, L. Ekstrom, E. Monsonego-Ornan, J. Ballantyne, P.E. Witten, C. Riley, W. Habraken, S. Omelon, Mineral homeostasis and regulation of mineralization processes in the skeletons of sharks, rays and relatives (Elasmobranchii), Semin. Cell Dev. Biol. 46 (2015) 51–57.
[31] M.R. Urist, Calcium and phosphrous in the blood and skeleton of the Elasmobranchii, Endocrinology 69 (4) (1961) 778–801.
[32] M. Hamada, T. Nagai, N. Kai, Y. Tanoue, H. Mae, M. Hashimoto, K. Miyoshi, H. Kumagai, K. Saiki, Inorganic constituents of bone of fish, Fish. Sci. 61 (3) (1995) 517–520.
[33] J.A. Freedman, D.L.G. Noakes, Why are there no really big bony fishes? A point-of-view on maximum body size in teleosts and elasmobranchs, Rev. Fish Biol. Fisheries 12 (4) (2002) 403–416.
[34] J.D. Currey, The design of mineralised hard tissues for their mechanical functions, J. Exp. Biol. 202 (23) (1999) 3285–3294.
[35] C. Rath, B. Janto, J. Earl, A. Ahmed, F. Hu, L. Hiller, M. Dahlgren, R. Kreft, F. Yu, J. Wolff, H. Kweon, M. Christiansen, K. Hakansson, R. Williams, G. Ehrlich, D. Sherman, Meta-omic characterization of the marine invertebrate microbial

consortium that produces the chemotherapeutic natural product ET-743, ACS Chem. Biol. 6 (11) (2011) 1244–1256.
[36] T.J. Pedley, S.J. Hill, Large-amplitude undulatory fish swimming: Fluid mechanics coupled to internal mechanics, J. Exp. Biol. 202 (23) (1999) 3431–3438.
[37] F.J. Plantema, Sandwich Construction: The Bending and Buckling of Sandwich Beams, Plates, and Shells, Wiley, New York, 1966.
[38] D. Zenkert, An Introduction to Sandwich Construction, Engineering Materials Advisory Services, 1995.
[39] A.P. Summers, T.J. Koob, The evolution of tendon – morphology and material properties, Comp. Biochem. Physiol. A: Mol. Integr. Physiol. 133 (4) (2002) 1159–1170.
[40] M.E. Porter, J.L. Beltran, T.J. Koob, A.P. Summers, Material properties and biochemical composition of mineralized vertebral cartilage in seven elasmobranch species (Chondrichthyes), J. Exp. Biol. 209 (15) (2006) 2920–2928.
[41] D.R. Huber, D.E. Neveu, C.M. Stinson, P.A. Anderson, I.K. Berzins, Mechanical properties of sand tiger shark (*Carcharias taurus*) vertebrae in relation to spinal deformity, J. Exp. Biol. 216 (22) (2013) 4256–4263.
[42] M.E. Porter, J.H. Long, Vertebrae in compression: Mechanical behavior of arches and centra in the gray smooth-hound shark (*Mustelus californicus*), J. Morphol. 271 (3) (2010) 366–375.
[43] C.A. Wilga, S.E. Diniz, P.R. Steele, J. Sudario-Cook, E.R. Dumont, L.A. Ferry, Ontogeny of feeding mechanics in smoothhound sharks: morphology and cartilage stiffness, Integr. Comp. Biol. 56 (3) (2016) 442–448.
[44] H.W. Courtland, G.M. Wright, R.G. Root, M.E. DeMont, Comparative equilibrium mechanical properties of bovine and lamprey cartilaginous tissues, J. Exp. Biol. 206 (8) (2003) 1397–1408.